Title

First Principles Study of Aluminum Doped Polycrystalline Silicon as a Potential Anode Candidate in Li-ion Batteries

Author

Bhimineni, Sree Harsha

Publication Date

2024

Peer reviewed|Thesis/dissertation

UNIVERSITY OF CALIFORNIA

Los Angeles

First Principles Study of Aluminum Doped Polycrystalline Silicon as a Potential Anode Candidate in Li-ion Batteries

A thesis submitted in partial satisfaction

of the requirements for the degree

Master of Science in Chemical Engineering

by

Sree Harsha Bhimineni

2024

ABSTRACT OF THE THESIS

First Principles Study of Aluminum Doped Polycrystalline Silicon as a Potential Anode Candidate in Li-ion Batteries

by

Sree Harsha Bhimineni

Master of Science in Chemical Engineering

University of California, Los Angeles, 2024

Professor Philippe Sautet, Chair

Energy storage remains a critical factor in the widespread adoption of renewable energy sources. While lithium-ion batteries have played a significant role, increasing their capacity using alternative materials is essential. In this context, microcrystalline silicon is a promising candidate for the anode due to its theoretically tenfold higher capacity compared to traditional graphite. However, its significant volume expansion during charge and discharge cycles hinders practical application due to mechanical breakdown and rapid loss of capacity. A novel approach to mitigate this issue is by incorporating trace amounts of aluminum into the micro-crystalline silicon electrode model. Density functional theory (DFT) is applied to establish a theoretical framework elucidating how grain boundary sliding, a key mechanism involved in preventing mechanical failure, is facilitated by the presence of trace aluminum at grain boundaries. This, in turn, reduces stress accumulation within the material, reducing the likelihood of failure. To validate the theoretical predictions, capacity retention experiments were performed on undoped and Al-doped micro-crystalline silicon samples by Shu-Ting Ko at the University of California San Diego (UCSD) in the research group of Prof. Jian Luo. The results demonstrate significantly reduced capacity fading in the doped sample, corroborating the theoretical framework and showcasing the potential of aluminum doping for improved Li-ion battery performance.

The thesis of Sree Harsha Bhimineni is approved.

Carlos Gilber Morales Guio

Yuzhang Li

Philippe Sautet, Committee Chair

University of California, Los Angeles

2024

Contents

LIST OF FIGURES

LIST OF TABLES

PREFACE

First, to Dr. Philippe Sautet, my sincere gratitude for your time, patience, and invaluable insights. Your guidance is instrumental in completing this work. Furthermore, I would like to dedicate this work to my parents, grandmother, and sister. Their belief in me and constant support have been a source of immense strength throughout my journey.

This work is funded by the Center for Synthetic Control Across Length Scales for Advancing Rechargeables (SCALAR), an Energy Frontier Research Center (EFRC) funded by the U.S. Department of Energy, Office of Science, Basic Energy Sciences (BES) under award DE-SC0019381.

This work utilized the computational and storage services of the Hoffman2 Shared Cluster provided by the UCLA Institute for Digital Research and Educational Research Technology Group (IDRE). I appreciate the computational time provided by Advanced Cyberinfrastructure Coordination Ecosystem: Services and Support's (ACCESS) San Diego Supercomputer Center's (SDSC) Expanse and Pittsburg Supercomputing Center's (PSC) Bridges2.

CHAPTER 1

Introduction

Lithium-ion batteries have become a norm for energy storage these days. Many advances to increase their efficiency have been proposed. In the realm of material science, electrode, electrolyte, and separator are interesting design elements. Specifically focusing on anodes, several materials are being explored such as graphitic materials, metals, metal oxides, and metal phosphide.[3] A key material explored is silicon. The obvious reason for silicon being a promising candidate is its high theoretical specific capacity (4200 mA-h/g for $Li_{22}Si_5$[4]) compared to the current graphite anode (372 mA-h/g[5]). Furthermore, silicon is the second-most abundant element in the earth's crust, making it a readily available material. However, its practical implementation is limited by a main bottleneck, the huge volumetric expansion after lithiation (310% for $Li_{22}Si_5$[6]) which causes a large build-up of stress, resulting in the pulverization of the material and immediate capacity loss during cycling[1,7–10] as shown in Figure 1.1.

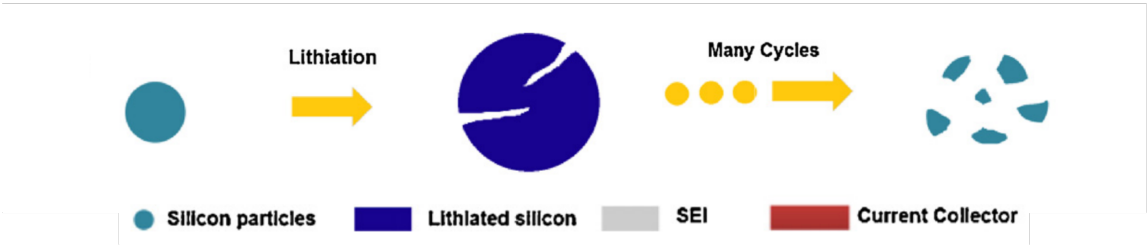

Figure 1.1: Pulverization of silicon particles in the anode during continuous cycling of the battery.[1]

An example is the loss of 70% of the capacity of silicon anode made from 10 μm silicon

powder within the first five cycles.[11] There has been a surge in research output to tackle this bottleneck over the past decade.[12] Specifically, one focus of research is on using micro-nano sized particle silicon anodes as they have been shown to resist cracking and accommodate the volumetric change.[12–14] However, the improvement is still not sufficient for practical application. Other cutting-edge research concentrates on modifying the anode by the formation of alloys,[15–17] composites,[18–20] core-shell structures,[21,22] films[23,24] and porous systems.[25,26]

Numerous theoretical investigations have been undertaken to address the challenges associated with lithium-ion battery performance. These studies predominantly focus on elucidating the intricacies of lithiation processes, lithium diffusivity, and the formation of the solid electrolyte interphase (SEI). Density functional theory (DFT) calculations have demonstrated a weakening of bonding strengths between adjacent silicon atoms upon lithiation,[27] while ab initio molecular dynamics simulations have provided insights into the transition from crystalline to amorphous phases during lithiation.[28] Investigations into the facet dependency of lithiation in silicon have revealed that the (110) surface exhibits superior thermodynamic stability compared to the (100) or (111) surfaces.[29] Furthermore, studies exploring the influence of oxygen content in silicon have revealed an inverse relationship between volume expansion and oxygen content.[30] First-principles calculations have been extended to examine lithiation in silicon-based composites, nanowires, and nanosheets.[31–34] For instance, ab initio simulations of Si/C hollow core-shell structures have provided valuable insights into interface adhesion and fracture behavior, informing the design of optimal core-shell structures.[32] Diffusivity studies provide fundamental data which is important for the design of electrodes. It has been demonstrated that aluminum doping up to a certain threshold (45 At%) enhances lithium diffusion,[35] while silicon nanosheets significantly promote lithium diffusivity.[34] The composition dependence of lithium diffusivity is investigated. It increases by two orders of magnitude with an increase in the lithium content, which can be explained by the instability of silicon, owing to charge transfer from lithium to silicon.[36] Regarding the solid electrolyte interphase, extensive literature exists, encompassing topics such as the decomposition of organic electrolyte components

on silicon surfaces and the influence of surface morphology on decomposition.[37–39] Additionally, numerous theoretical studies have focused on in vivo (SEI modification during cycling) and in vitro (surface coating layer design) SEI modifications[40] to make it more stable during cycling conditions.

On the fundamental aspect, unavoidable volume expansion in each crystalline grain of silicon upon lithiation creates important mechanical stress in the material, responsible for rupture. A major mechanism to relieve this stress would be to allow facile sliding at the grain boundaries (GBs).[41,42] Previous experimental observations of GB sliding have been predominantly limited to metallic materials such as Al, Cu, Sn, Zn, and Mg.[43–47] Based on current knowledge, there has been no work in the literature on GB sliding in silicon. This comes from the fact that silicon has strong covalent bonds, which may render GB sliding highly activated and inoperative at near ambient temperature. In this manuscript, GB sliding in silicon is studied using first-principle atomistic simulations. GB sliding in silicon is shown to be activated and doping silicon with aluminum markedly facilitates GB sliding, and is, therefore, a potential solution to improve the mechanical properties and durability of silicon anodes upon cycling. It is shown that the small amount of aluminum segregates in the grain boundaries of silicon and greatly facilitates GB sliding. The prevalence of the $\Sigma 3$ $\{111\}$ GB in polycrystalline materials has been well-documented in numerous previous studies[48–50] and is revealed in the GB characteristics quantification by electron backscattered diffraction performed by Shu-Ting Ko at the University of California San Diego in the research group of Prof. Jian Luo as shown in Figure 1.2. Recognizing its significance, $\Sigma 3$ $\{111\}$ GB is consistently employed in all the simulations. A unique model is devised to perform grain boundary sliding simulations. The investigative approach encompasses the utilization of basin hopping, a global optimization technique to understand the segregation of aluminum in the GB. This computational framework is used to gain insights into the influence of aluminum on GB sliding behavior, hence enabling the reorganization of the polycrystalline silicon anode without mechanical failure during lithiation. The simulation results are validated through experiments performed by Shu-Ting Ko at the University of Cal-

ifornia San Diego in the research group of Prof. Jian Luo. Micro-sized polycrystalline silicon is experimentally doped with 5 wt.% (4.9 mol.%) aluminum and mixed by high-energy ball milling. Using a charge-discharge cycling test of half cells, the aluminum-doped silicon anode is shown to exhibit improved capacity retention than the undoped counterpart. This approach provides an innovative and cost-effective way of improving the cyclic stability of silicon anodes.

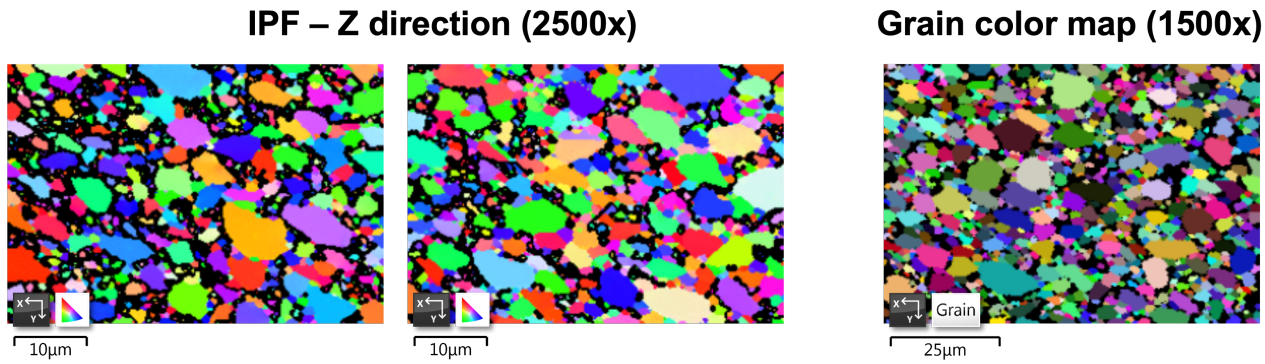

(a)

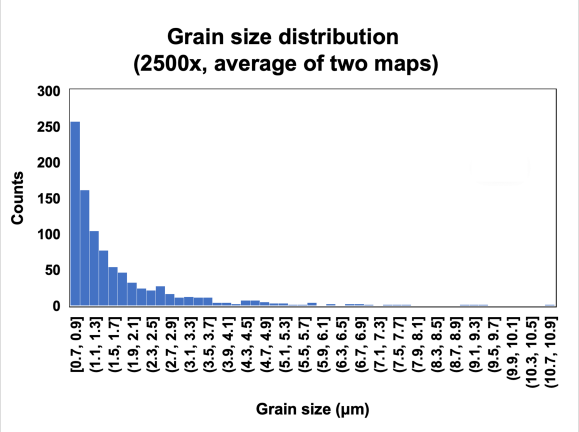

(b)

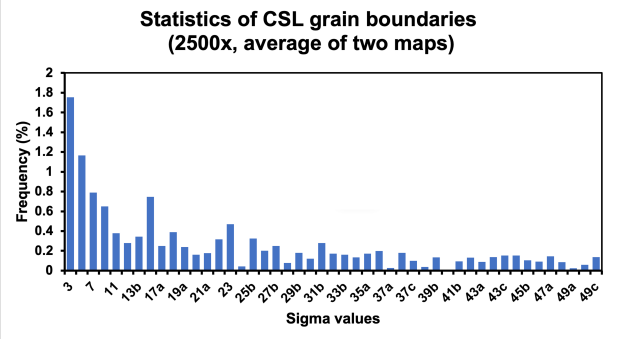

(c)

Figure 1.2: Electron back-scattered diffraction (EBSD) characterization of the silicon sample used for experiments. (a) Inverse pole figures (IPF) in the Z direction and grain color map; (b) Grain size distribution represented in intervals of 0.2 µm indicating micro-sized particles in the sample and (c) Statistics of the coincidence site lattice (CSL) grain boundaries indicating that the Σ3 GB is the most frequent one in the sample.

The thesis is organized as follows. Chapter 1 focuses on the importance of silicon as an anode for Li-ion batteries, discusses the bottlenecks in practical application, and suggests possible solutions. One of the possible solutions, which is doping the anode with aluminum, will be discussed in this thesis. Chapter 2 explains all the methods and models used to make this work possible which are density functional theory (DFT), coincidence site lattice model (CSL) for GBs, basin hopping (BH) for understanding the segregation of aluminum in the GB and GB sliding model. In Chapter 3, the validity of the devised GB sliding model is established by comparing it with existing literature. In Chapter 4, the effect of aluminum on GB sliding is studied and compared with the case without aluminum. Chapter 5 validates the conclusions obtained from simulations using the experimental cyclic stability test performed by Shu-Ting Ko at the University of California San Diego in the research group of Prof. Jian Luo. Summary and conclusion are discussed in Chapter 6. The results from this thesis are published in ChemRxiv titled "First Principles Study of Aluminum Doped Polycrystalline Silicon as a Potential Anode Candidate in Li-ion Batteries"[51] authored by Sree Harsha Bhimineni, Shu-Ting Ko, Yantao Xia, Jian Luo and Philippe Sautet.

CHAPTER 2

Methods

2.1 Energy Calculations

All electronic energy calculations are performed with Density Functional Theory (DFT), implemented using the Vienna ab initio simulation package (VASP).[52] The atomic simulation environment (ASE)[53] is used in conjunction with VASP to develop custom automation scripts in Python which are available at GitHub.[54] The electron-ion interactions are treated using the projected augmented wave (PAW) method. The exchange-correlation effects are incorporated using the Perdew-Burke-Ernzerhof (PBE) functional.[55] The Brillouin-zone integration is performed using Monkhorst pack[56] k-point grids of 13x13x13 for bulk calculations and 15x9x1 for GB calculations. To improve the convergence of the calculation with respect to the k-points, tetrahedron smearing with Blöchl corrections is used. The valence electrons are considered as a set of plane waves according to the Bloch theorem with a cutoff energy of 300 eV. All the structures are geometrically optimized using the conjugate gradient algorithm until the force on each atom is less than 0.01 eV/Å.

2.2 Generation of Grain Boundary

For two grains misoriented by a rotation angle about a rotation axis, the superposition of the two crystals results in coincident sites forming a sublattice of the two crystal lattices. A grain boundary can be completely described by 5 degrees of freedom (DoFs). 3 DoFs are for the

crystallographic orientation of one grain relative to the other and 2 DoFs are for the orientation of the boundary relative to one of the grains, that is, the GB plane.[57,58]

$$\Sigma 5\ 36.87^{o}/[100](031) \tag{2.1}$$

where $\Sigma 5$ describes the reciprocal of the density of coincident sites (it implies 1/5th of the atoms are in coincident sites[58]), [100] describes the rotation axis, (031) describes the grain boundary plane, and 36.87° represents the rotation angle. The lesser the Σ, the lesser are the misorientations. GBs generated through the CSL model mostly have low energy. There are grain boundaries that do not follow the CSL model which are called general GBs.

The $\Sigma 3$ 60°/[111](111) GB, abbreviated as the $\Sigma 3$ {111} GB, can be described as a twist boundary characterized by a layered structure. In this GB, each grain's top and bottom layers are derived from bulk silicon with a relative twist angle of 60° between them. The bicrystal model of GB has been implemented. Subsequently, layers from each grain are systematically stacked atop one another through the custom Python script.[54] One notable advantage of this approach is the precise control it provides over the number of layers within each grain, allowing for tailored investigations. The GB is characterized by its interface energy which is defined according to Equation 2.2.

$$E_{GB}^{I} = \frac{E_{GB} - n_{Si}E_{BulkSi} - n_{Al}E_{BulkAl}}{2A} \tag{2.2}$$

where E_{GB}^{I} is the interface energy of the GB, E_{GB} is the energy of the GB supercell, n_{Si} is the number of silicon atoms in the GB, E_{BulkSi} is the per atom energy of bulk diamond cubic silicon, n_{Al} is the number of aluminum atoms in the GB, E_{BulkAl} is the per atom energy of bulk fcc aluminum and A is the interface area of the GB. The factor 2 is incorporated to indicate the presence of two GBs in the unit cell.

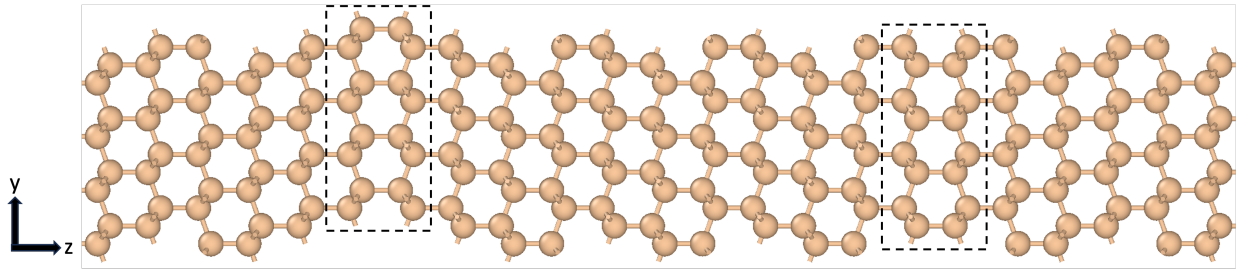

Figure 2.1: Model of the Σ3 {111} GB with orthorhombic supercell repeated in the y direction. The dashed boxes indicate the grain boundaries. The grain boundaries are separated by 11 layers in this model.

2.3 Aluminum Segregation Exploration

In order to obtain the most stable configuration for the aluminum segregation in the GB, the Basin Hopping algorithm is used which is based on the canonical Monte Carlo technique[59] as shown in Figure 2.2, where the algorithm alters the coordinates of the current structure to a new structure according to predefined constraints called modifiers and then geometrically optimizes it. The optimized new structure can be accepted or rejected based on the Metropolis criterion.[60] The results are interpreted using aluminum insertion energy as defined in Equation 2.3. The decision to employ the basin-hopping technique in this research is inspired by the work of Sun *et al*. In their study, Sun *et al*. successfully applied this method to investigate the behavior of a Pt_8 cluster on an alumina substrate under varying hydrogen pressures.[61]

$$E_{Al} = E_{GB+nAl} - E_{GB} - n_{Al}E_{BulkAl} \tag{2.3}$$

where E_{Al} is the aluminum insertion energy, E_{GB+nAl} is the energy of the grain boundary with substituted alumina, n_{Al} is the number of substituted alumina, E_{GB} is the energy of the GB without alumina and E_{BulkAl} is the per atom energy of bulk fcc aluminum.

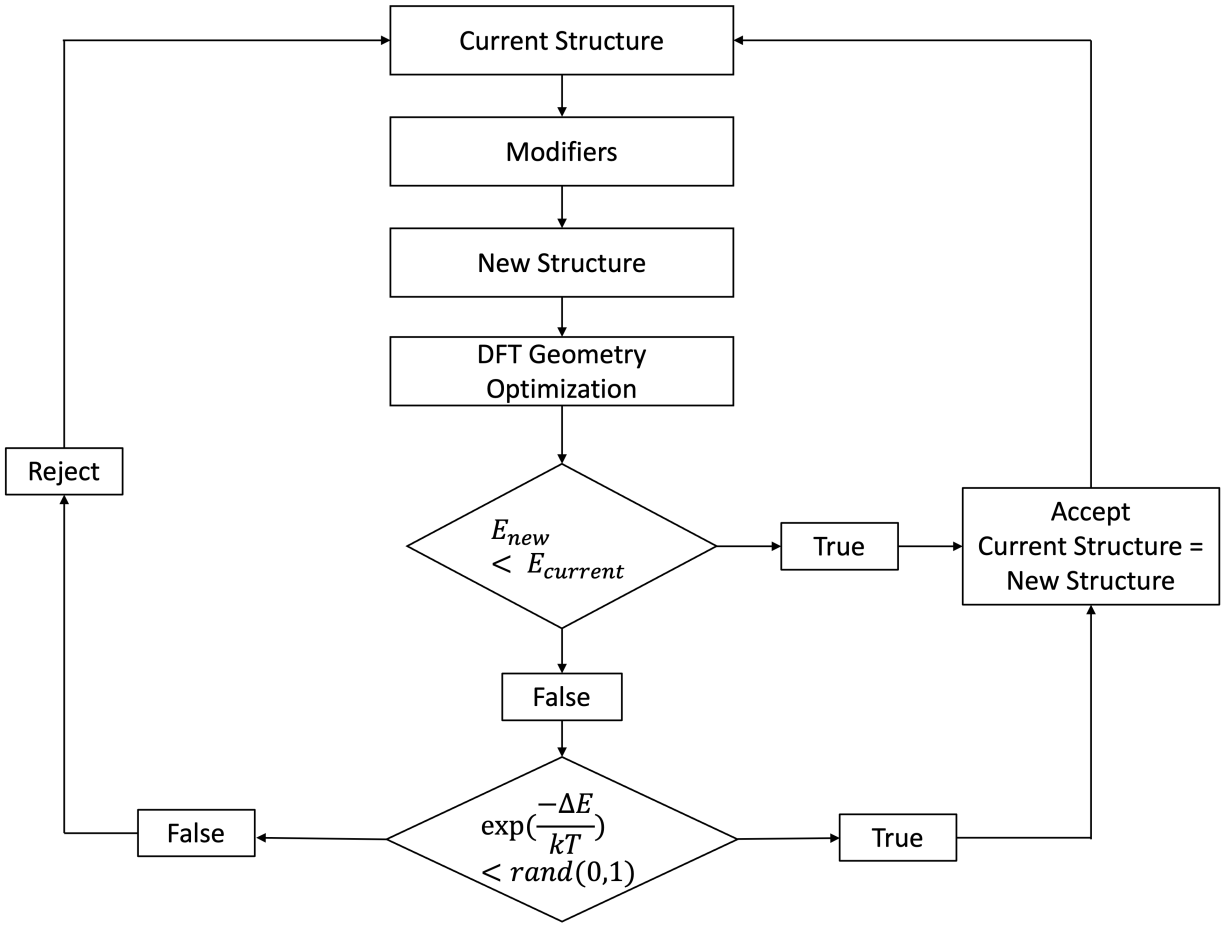

Figure 2.2: Flowchart explaining the Basin Hopping algorithm. The new structure is accepted or rejected based on the Metropolis criterion. ΔE is the difference of aluminum insertion energy between the new structure and the current structure (E_{new} - $E_{current}$).

2.4 Grain Boundary Sliding

The dominant phenomenon observed during mechanical operations at grain boundaries is known as GB sliding. To gain insights into how the segregation of aluminum at GB influences this phenomenon, a comprehensive study of GB sliding becomes imperative. As a result, a model is developed through a custom Python script.[54] In this approach, one layer is fixed within each of the grains, preventing any atomic position relaxation. Employing a systematic, serial methodology, relative displacements are introduced between the layers of one grain to the other. Subsequently, the resulting atomic structure is subjected to geometric optimization. These fixed

layers effectively serve as constraints, maintaining the deformation within the GB region.

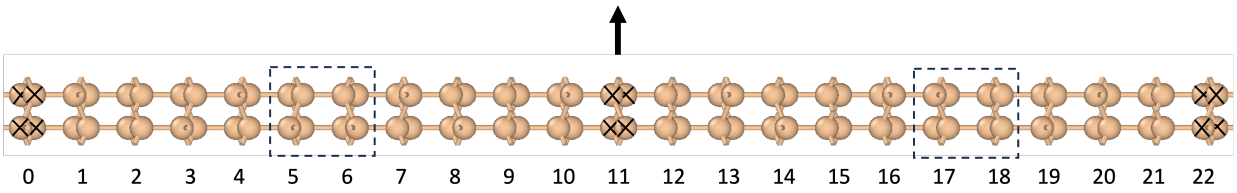

Figure 2.3: Schematic diagram of Σ3{111} GB unit cell including 11 layers per grain. The dashed boxes indicate GBs, cross marks indicate the atoms that are fixed, arrow mark indicates the direction of sliding and the numbers indicate the layer index.

CHAPTER 3

GB Sliding

The calculated lattice parameter of bulk silicon is $a = b = c = 5.43$ Å, which is in agreement with experiments.[62] In all the simulations, an 11-layered (11 layers per grain) $\Sigma 3$ $\{111\}$ GB structure with the orthorhombic unit cell as described in Section 2.2 is examined, with $a =$ 3.866 Å, $b = 6.697$ Å and $c = 69.454$ Å, characterized by an interface energy of 1.5 meV/Å^2 agreeing with experimental observations documented in the literature.[63]

Using the algorithm detailed in Section 2.4, simulations are conducted to investigate GB sliding initially using the model of Figure 2.1 and 2.3 where the GBs are separated by 11 silicon layers. The simulation spanned 20 steps, with each step corresponding to a relative displacement of 0.773 Å (equivalent to one-fifth of the unit cell length in the x-direction, measuring 3.866 Å). Figure 3.1a illustrates the initial steps characterized by elastic deformation, where no significant bond restructuring occurs, signifying the absence of sliding. This elastic deformation accumulates stress within the structure, eventually leading to stress release through a sliding event between the relative displacement of 8.506 Å and 9.279 Å (steps 11 and 12 respectively). Notably, this sliding occurs between layers 5 and 6 as can be seen in Figure 3.1b, as well as 17 and 18, which are the grain boundary layers, as depicted in Figure 2.3. This observation is documented in several previous studies on other materials and has been termed as a saw-tooth mechanism or stick-slip mechanism.[64,65] This validates the accuracy of the model in reflecting GB sliding behavior.

In this context, the barrier for GB sliding (ΔE) is defined, as expressed in Equation 3.1.

$$\Delta E = E[max] - E[min] \tag{3.1}$$

Here, $E[min]$ corresponds to the interface energy of the GB without deformation, while $E[max]$ corresponds to the maximum interface energy of the GB along the deformation.

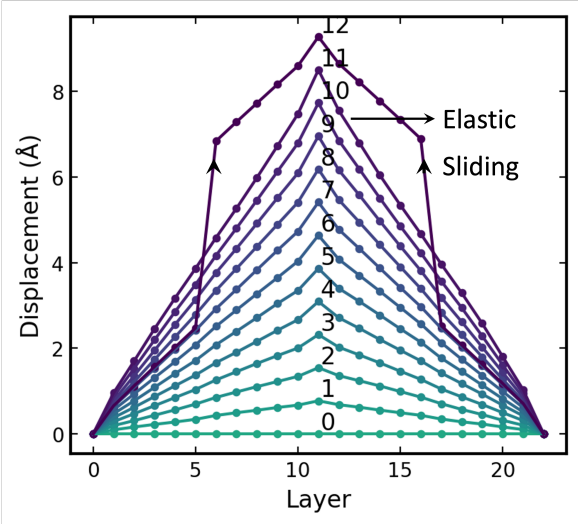

(a)

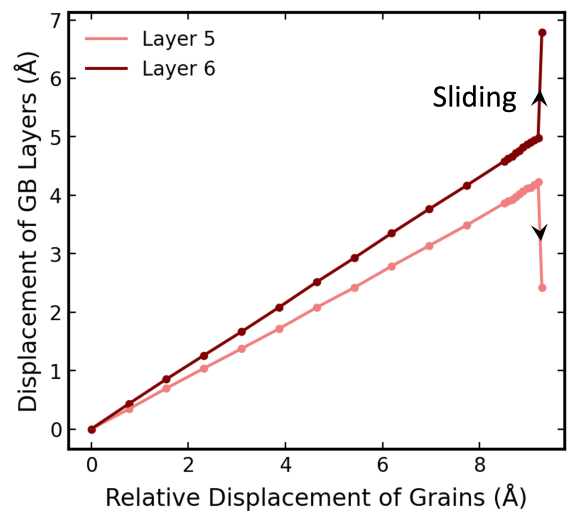

(b)

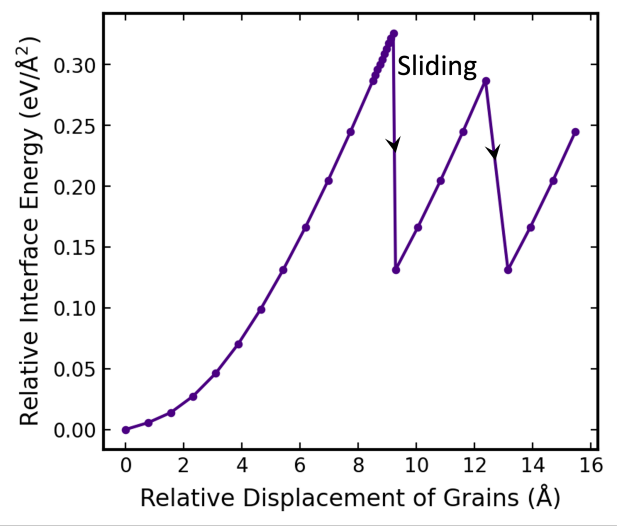

(c)

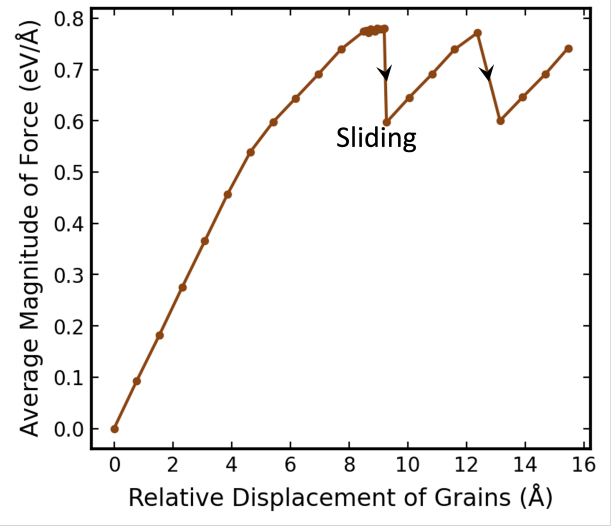

(d)

Figure 3.1: GB sliding simulations for the Σ3 {111} GB with 11 silicon layers between the GBs. (a) Displacement as a function of the layer index with increasing relative displacement between grains. Layers 0, 11 and 22 are kept fixed, while the layer 11 is displaced (See Figure 2.3 for the structure). The step number is indicated on each line where each step corresponds to a relative displacement of 0.773 Å; (b) Displacement of the 5th and 6th layers (GB layers) with increasing relative displacement between the grains including the ten simulations with a finer displacement of 0.077 Å between the relative displacement of 8.506 Å and 9.279 Å; (c) Relative interface energy (the difference between interface energy and interface energy of undeformed GB) versus the relative displacement between the grains including the ten simulations with a finer displacement of 0.077 Å between the relative displacement of 8.506 Å and 9.279 Å; and (d) Average magnitude of force experienced by the atoms that are fixed in layer 0, 11 and 21 (refer Figure 2.3) as a function of relative displacement of the grains including the ten simulations with a finer displacement of 0.077 Å between the relative displacement of 8.506 Å and 9.279 Å.

To obtain an accurate value of ΔE, ten GB sliding simulations are performed (with a smaller step corresponding to a displacement of 0.077 Å) between the relative displacement of 8.506 Å and 9.279 Å as shown in Figure 3.1c. A lower barrier indicates greater ease of sliding and more effective stress release. However, in the current case, the sliding barrier measures 0.33 eV/Å^2, which is 220 times that of the interface energy of the undeformed GB. This implies a high degree of rigidity in sliding and a consequently elevated risk of structural cracking. Apart from the energetics, since the atoms in layers 0, 11, and 21 are fixed as shown in Figure 2.3, they experience a non-zero force when the GB is deformed. The average magnitude of force on the fixed atoms is represented in Figure 3.1d. This force drops at a relative displacement of 9.279 Å which coincides with the GB sliding. However, the structure and its energy do not return to that of the undeformed state as can be seen in Figure 3.1a and 3.1c. Sliding stops at a partially deformed structure, indicating that the stress release is not effective during sliding.

CHAPTER 4

Effect of Aluminum on GB Sliding

4.1 Understanding the Segregation of Aluminum

The investigation is first aimed at understanding the underlying principles governing aluminum segregation within the GB system. An important observation is that aluminum exhibits a significant preference for the substitutional site (0.99 eV) over the interstitial site (2.77 eV) in bulk silicon. Furthermore, results from simulations indicate that it is energetically more favorable for aluminum to occupy the grain boundary substitutional site (0.9 eV) compared to the bulk site (0.99 eV). All these values are summarized in Table 4.1. This intriguing behavior implies that aluminum's segregation tendency is profoundly influenced by the grain boundary environment.

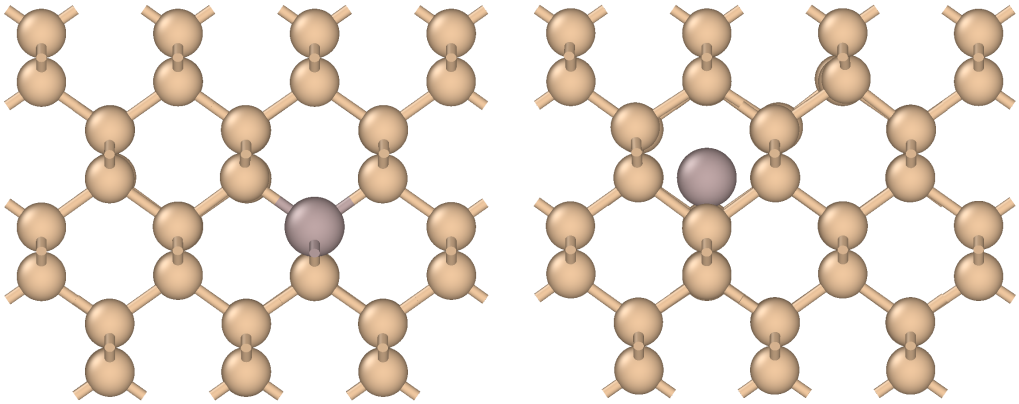

(a) **(b)**

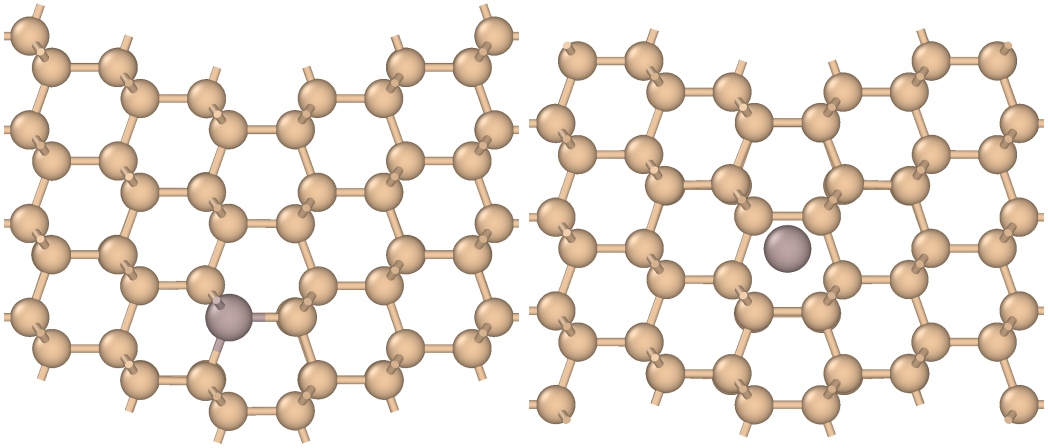

(c) **(d)**

Figure 4.1: Insertion of aluminum in bulk and GB structures of silicon. (a) Aluminum in the substitution site of bulk silicon; (b) Aluminum in the interstice site of bulk silicon; (c) Aluminum in the substitution site of the GB of silicon and (d) Aluminum in the interstice site of the GB of silicon.

Site	Aluminum Insertion Energy (eV)
Bulk Substitution	0.99
Bulk Interstice	2.77
GB Substitution	0.9
GB Interstice	2.22

Table 4.1: Aluminum insertion energies for different sites in silicon bulk and GB structures.

It is noteworthy that despite the positive insertion energy of aluminum within silicon, a prediction aligned with the phase diagram as shown in Figure 4.2,[2] the unique conditions imposed by the ball milling process, employed in the sample preparation, facilitate the exploration of higher energy states and the creation of metastable structures with well-dispersed aluminum.

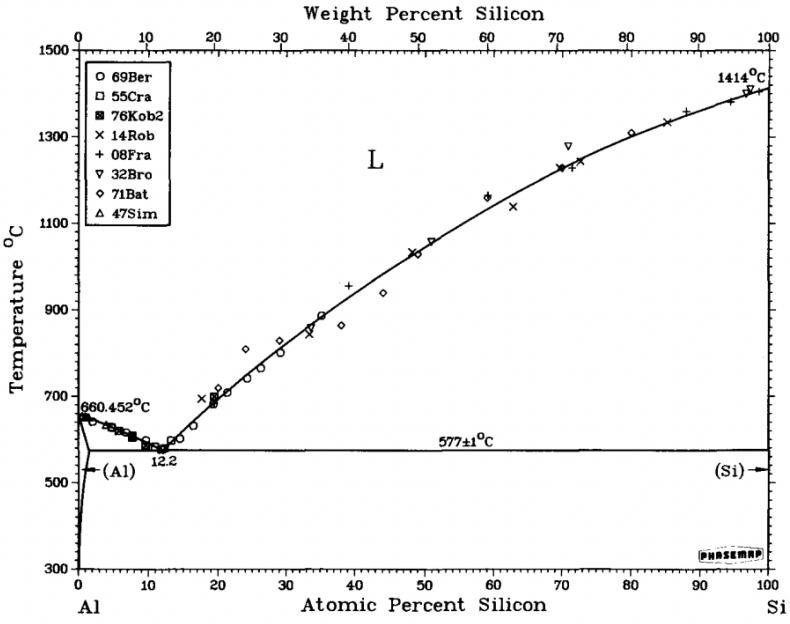

Figure 4.2: Phase diagram of Silicon and Aluminum.[2]

A notable condition is the presence of trace oxygen in the ball milling environment, which promotes the segregation of aluminum at the interface. This is proved by the simulations with systems containing aluminum and oxygen at the GB as shown in Figure 4.4. It is to be noted that the reference for oxygen for calculating aluminum insertion energy is oxygen in the interstice position of bulk and/or GB according to the oxygen's position as shown in Figure 4.3.

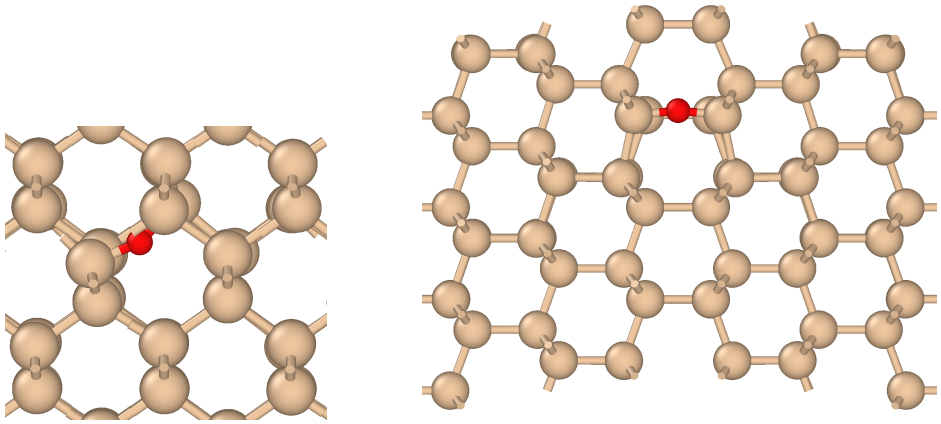

(a) **(b)**

Figure 4.3: Schematic of oxygen in (a) The interstice site of bulk of silicon and (b) The interstice site of the GB of silicon.

With one oxygen atom surrounding each substituted aluminum atom, the aluminum insertion energy has dropped to 0.77 eV from 0.9 eV. It further drops to negative values in the presence of more oxygen as represented in Table 4.2. In comparison, for bulk, the aluminum insertion energy only drops to 0.92 eV from 0.99 eV. This implies that the presence of trace oxygen would make it thermodynamically favorable for aluminum to segregate in the GB. However, the presence of oxygen is not going to be accounted for in the sliding simulations, which comes from the rationale that the oxygen is removed from the anode due to the presence of reductive conditions during the cycling of the battery. Furthermore, it is found that the oxygen preferentially interacts with the incoming lithium during cycling of the battery, which further promotes the chances of the removal of oxygen.[30] This implies that the aluminum is left behind at a metastable state.

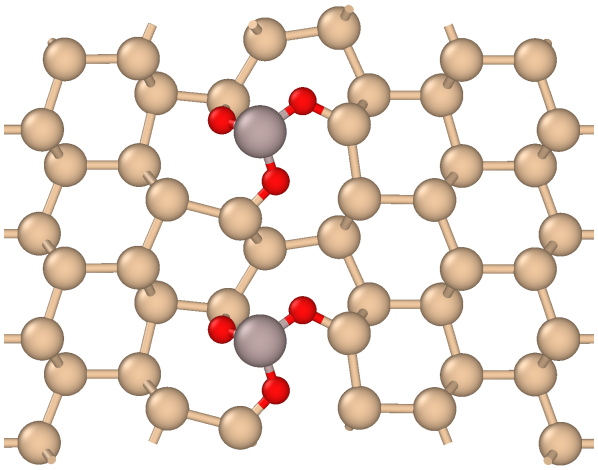

Figure 4.4: Schematic of substituted aluminum bonding with three surrounding interstice oxygen atoms (in which two are bulk oxygen atoms and one is GB oxygen atom). The oxygen atoms occupy bridging positions between aluminum and neighboring silicon atoms.

Number of oxygen atoms	Aluminum insertion energy in GB (eV)	Aluminum insertion energy in bulk (eV)
0	0.9	0.99
1	0.77	0.92
2	0.20	0.42
3	-0.27	-0.18
4	-0.82	-0.67

Table 4.2: Aluminum insertion energy of GB substituted aluminum for different numbers of surrounding oxygen atoms.

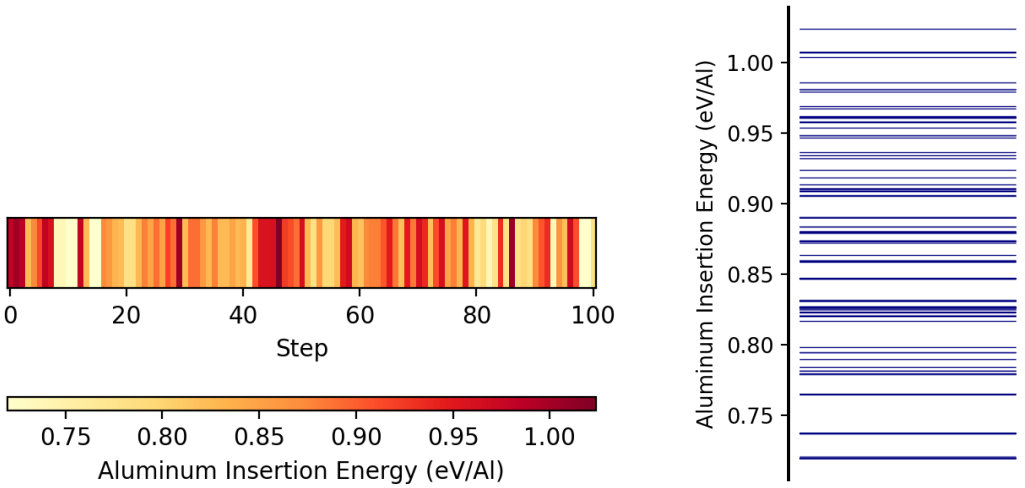

(a) **(b)**

Figure 4.5: Basin hopping simulation results for the segregation of aluminum in GB. This figure corresponds to the case where there are 4 aluminum per GB. (a) Aluminum insertion energy as a function of the basin hopping step. (b) Different aluminum insertion energies explored in the basin hopping run.

Furthermore, basin hopping as described in Section 2.3 is used to understand the segregation of multiple aluminum atoms in the GB, for up to 4 aluminum per GB. Aluminum is allowed

to substitute in place of GB silicon atoms. The number of aluminum substituted and their positions are chosen randomly in each step. Each basin hopping is run for 100 steps. The results of basin hopping for the 4 aluminum per GB case are represented in Figure 4.5. From Figure 4.5a, it can be observed that higher energy states are attained throughout the run, switching from one to the other, enabling a wide exploration window. Moreover, a broad range of energies (0.7 eV - 1.1 eV) are covered in the run as can be seen in Figure 4.5b. The resulting global minimum has a characteristic feature, i.e., all the aluminum are in a single layer. This is a consequence of the phase diagram of silicon-aluminum, where aluminum has very low solubility in silicon, and therefore aluminum atoms prefer to accumulate together.

4.2 GB Sliding with Aluminum

After identifying the optimal aluminum segregation configurations for different numbers of aluminum, the subsequent step involved conducting GB sliding simulations using these configurations. Each simulation consisted of 20 steps, with each step corresponding to a relative displacement of 0.773 Å, similar to the one used for pure Si GB. The results from GB sliding simulations for the scenario with four aluminum atoms per GB are visually presented in Figure 4.6.

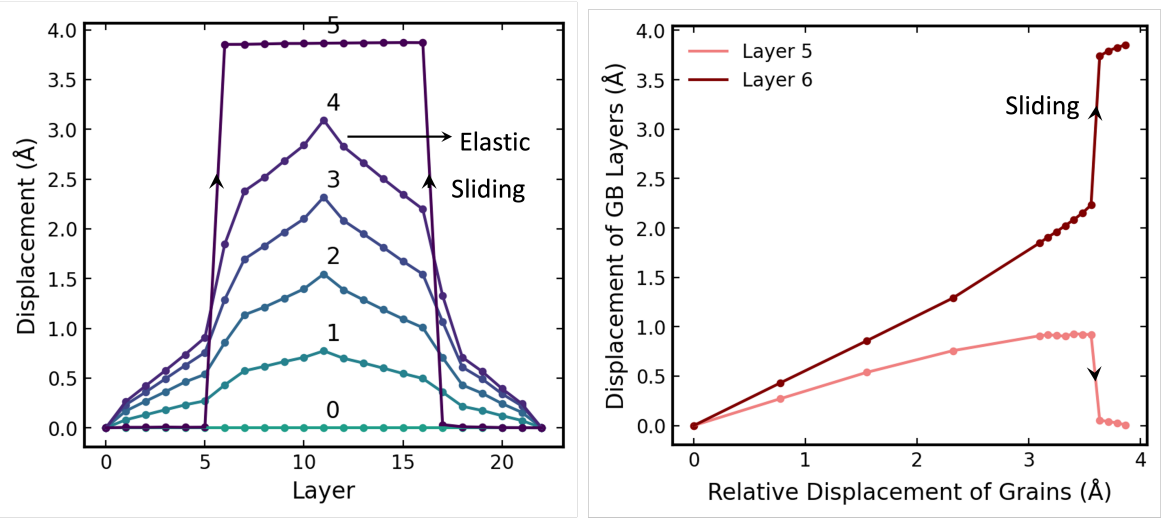

(a) **(b)**

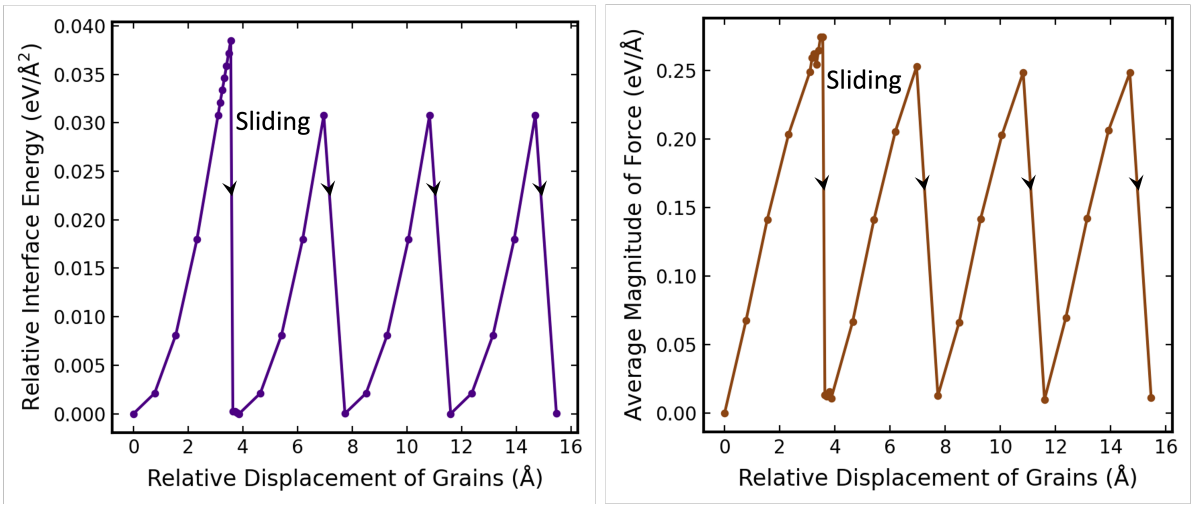

(c) **(d)**

Figure 4.6: GB sliding simulations for the Σ3 {111} GB with 11 silicon layers between the GBs and 4 Al per GB. (a) Displacement as a function of the layer index with increasing relative displacement between grains. Layers 0, 11 and 22 are kept fixed, while the layer 11 is displaced (See Figure 2.3 for the structure). The step number is indicated on each line where each step corresponds to a relative displacement of 0.773 Å; (b) Displacement of the 5th and 6th layers (GB layers) with increasing relative displacement between the grains; (c) Relative interface energy (the difference between interface energy and interface energy of undeformed GB) versus the relative displacement between the grains including the ten simulations with a finer displacement of 0.077 Å between the relative displacement of 3.557 Å and 3.634 Å, and (d) Average magnitude of force experienced by the atoms that are fixed in layer 0, 11 and 21 (refer Figure 2.3) as a function of relative displacement of the grains including the ten simulations with a finer displacement of 0.077 Å between the relative displacement of 3.557 Å and 3.634 Å.

Several significant differences between GB sliding with and without aluminum are discernible: (a) The sliding barrier is remarkably lowered to 0.0385 eV/Å^2, representing about 12% of the case without aluminum as can be seen in Figure 4.6c. Moreover, this value is merely 40% of the interface energy of the undeformed GB with aluminum. (b) The peak force of the

system with aluminum has dropped by 66 % in comparison to the system without aluminum as shown in Figure 4.6d. This reduction suggests that the presence of aluminum mitigates the rigidity of the GB, enabling sliding, contributing to effective stress relief, and, ultimately, the prevention of mechanical failure; (c) In contrast to sliding without aluminum, the frequency of sliding is notably higher. Sliding occurred at a relative displacement of 3.634 Å, compared to a relative displacement of 9.279 Å in the absence of aluminum, as depicted in Figure 4.6b. This increased sliding frequency plays a crucial role in averting the accumulation of excessive stress in the material and (d) Following each sliding event, the GB rapidly returned to its completely undeformed state. This observation indicates substantial stress alleviation due to the presence of aluminum. These findings collectively validate the hypothesis that aluminum facilitates GB sliding, thereby reducing the likelihood of mechanical failure within the material.

The observed outcomes are contingent on the aluminum content per grain boundary (GB). However, the influence of the number of aluminum atoms at the GB on the sliding behavior exhibits a nuanced pattern, graphically represented in Figure 4.7. The introduction of one aluminum per GB yields a substantial 49% reduction in the sliding barrier. The introduction of second and third aluminum per GB further decreases the barrier by 18% and 21% respectively. However, when the aluminum content increases from 3 to 4 atoms per GB, the sliding barrier is more or less stable and diminishes with a mere decrease of 0.3%. This suggests that beyond a certain threshold, additional aluminum content has only a minor impact on GB sliding. Another crucial factor to consider is the concurrent increase in interface energy with rising aluminum content. This counters the reduction in the sliding barrier attributed to aluminum's presence by making the initial interface formation more challenging. Therefore, selecting the optimal aluminum content in the silicon anode entails a delicate balance between reducing the sliding barrier and managing the associated increase in interface energy.

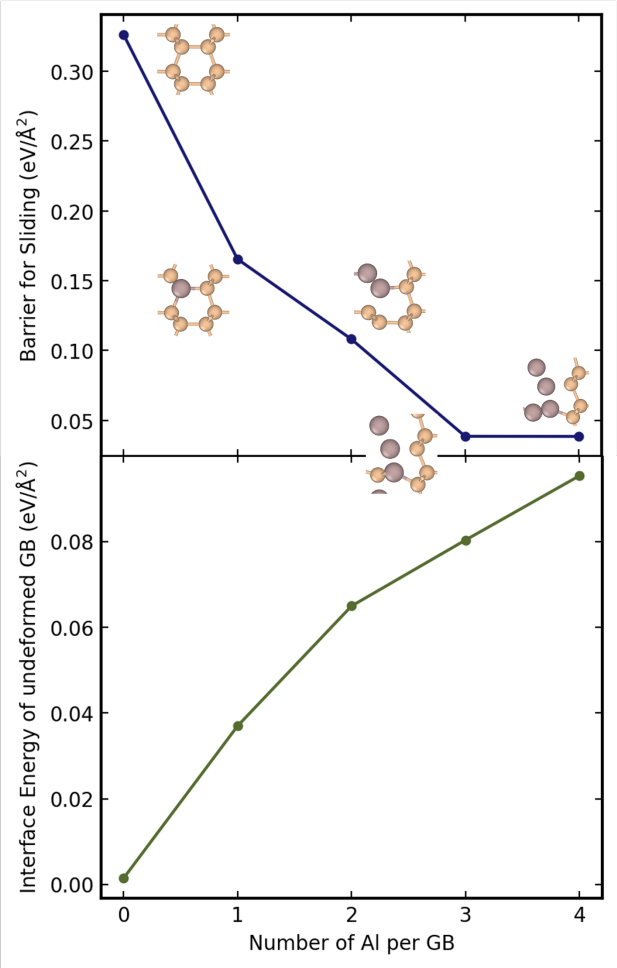

Figure 4.7: Effect of aluminum content on GB sliding and interface energy. The grey spheres indicate aluminum and the yellow spheres indicate silicon. Top: Barrier for sliding versus the number of aluminum per GB and Bottom: Interface energy of undeformed GB versus the number of aluminum per GB.

4.3 Effect of Number of Layers on GB Sliding

To understand the effect of the number of layers in the GB model, simulations are performed with values ranging from 7 to 13 layers per grain for systems with and without aluminum. The results are graphically represented in Figure 4.8a. Analysis revealed that the maximum force required to initiate GB sliding remained consistent across all the structures with the same number of aluminum per GB. This observation implies that the number of layers within the GB has no discernible impact on the sliding behavior. However, there are interesting differences between the structures with and without aluminum as represented in Figure 4.8. First, the maximum displacement of grains before sliding increases with the number of layers and is hence not an intrinsic parameter describing the sliding. This is because a specific displacement per layer is required to induce the shear (or force) for GB sliding. Furthermore, from Figure 4.8c, the reduction in slope indicates that the maximum relative displacement of grains before the sliding event occurred became a weaker function of the number of layers when aluminum is added to the system. A notable observation for systems with aluminum is, that even though there is an increasing amount of rigid Si-Si bonds as the number of layers per GB increases, this has no significant impact on the sliding indicating that the aluminum at the GB plays a major role in facilitating sliding. In the presence of Al at the GB, a displacement between grains results in an equivalent shear at the GB interface because this is the weakest part. In the case of pure silicon, the deformation is distributed within the grain and at the GB interface.

4.4 Understanding Bonding in the GB using COHP

To delve into the underlying chemical mechanisms governing the impact of aluminum on grain boundary (GB) sliding, Crystal Orbital Hamilton Population (COHP) analysis is utilized, facilitated by the Local-Orbital Basis Suite Towards Electronic Structure Reconstruction (LOBSTER) code.[66] This analytical approach provides insights into the atomic bonding interactions within a given structure, with particular emphasis on the quantification of bond strength

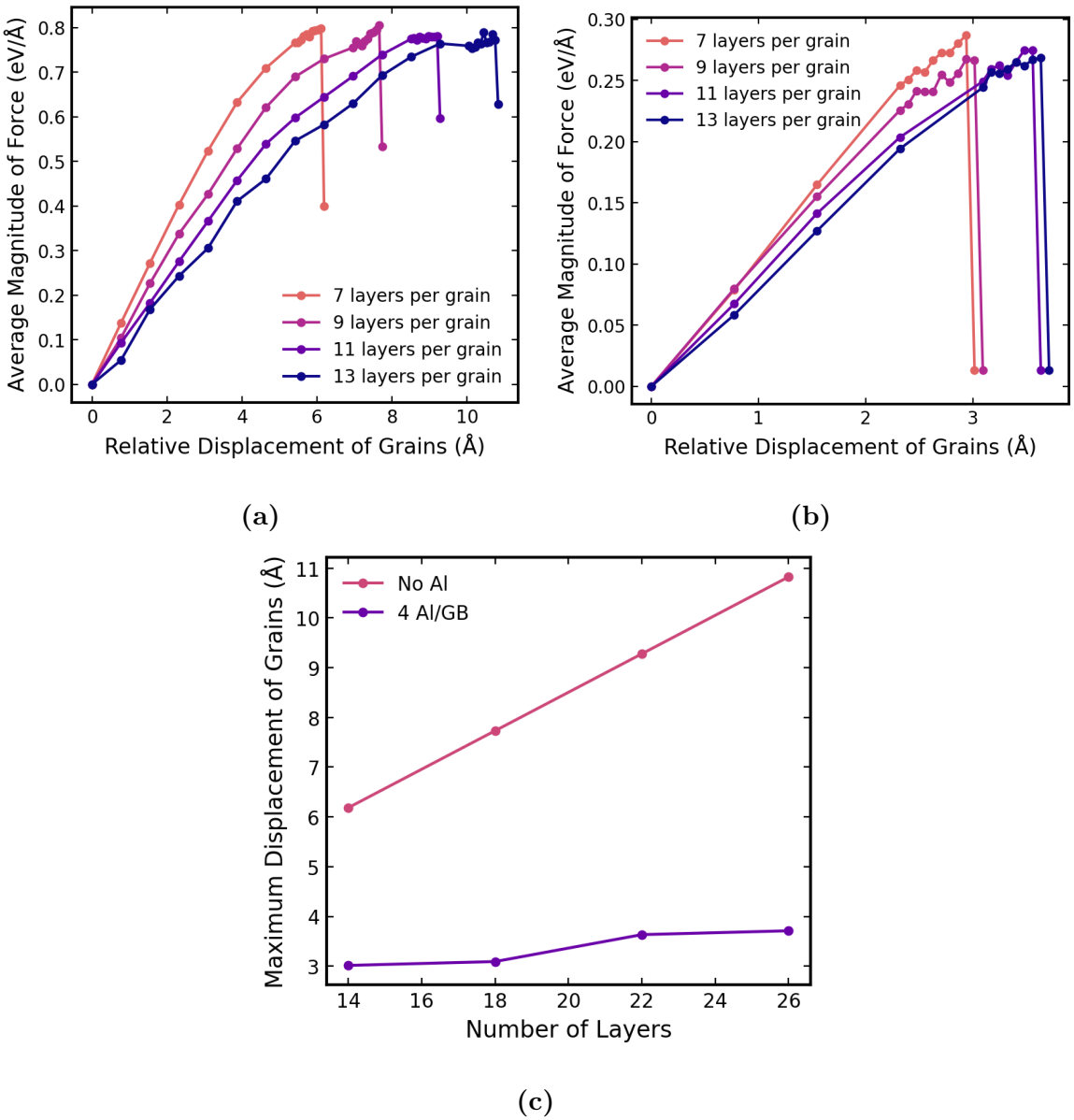

Figure 4.8: The effect of the number of layers on GB sliding. (a) The average magnitude of force experienced by the atoms that are fixed versus the relative displacement of grains for different layered GB structures, (b) The average magnitude of force experienced by the atoms that are fixed versus the relative displacement of grains for different layered GB structures with 4 Al per GB, and (c) The maximum relative displacement of grains as a function of number of layers in the GB for systems without and with aluminum.

through Integrated COHP (ICOHP) values. A higher ICOHP value signifies a stronger bond. In the absence of aluminum, the sole bonds present in the GB are Si-Si bonds, which exhibit an ICOHP value of 4.380. However, when aluminum is introduced at the GB, the landscape shifts. Some Si-Si bonds are supplanted by Al-Si bonds, characterized by an ICOHP value of 3.774, indicative of weaker binding. Furthermore, the bonding states for Si-Si are comparatively higher than the bonding states of Al-Si (refer to the green area in Figure 4.9). This contrast highlights the weaker nature of Al-Si bonds in comparison to their Si-Si counterparts. Consequently, this disparity in bond strength facilitates more facile bond reconstructions during GB sliding, a phenomenon akin to a lubricating effect induced by the presence of aluminum.

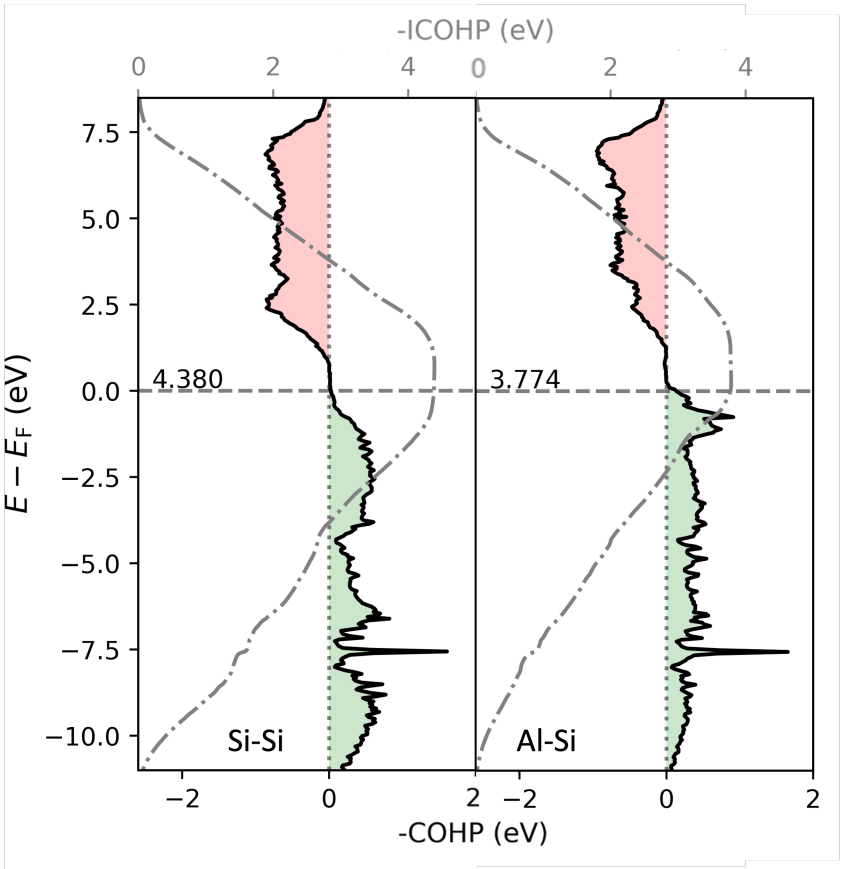

Figure 4.9: COHP (solid line) and ICOHP (dash-dot line) curves versus one-electron energy (using the traditional x(y) representation). Left: Si-Si bonds at the GB for the pure Si case and Right: Al-Si bonds. The green area signifies bonding states and the red area signifies anti-bonding states. Only bonding states are populated.

CHAPTER 5

Experimental Validation Performed by Shu-Ting Ko at UCSD

Shu-Ting Ko has performed the experiments at the University of California San Diego in the research group of Prof. Jian Luo. The prepared Al-doped Si anode exhibits enhanced capacity retention up to 43.22% at 50 cycles in the cycling stability test at 0.1 C, which outperforms the retention percentage of pristine Si anode (27.68%), shown in Figure 5.1a and 5.1b. The coulombic efficiency of Al-doped Si anode reaches 97.02% at the 5^{th} cycle (versus 95.51% of pristine Si), which indicates improved reversibility of the chemical reactions. The morphology and primary particle size of the Al-doped and undoped Si samples are similar as observed from SEM images in Figures 5.1c and 5.1d insets. However, the Al-doped Si shows a higher initial specific discharged capacity of 3166.9 mAh/g compared to pristine Si and also less decay within the first 30 cycles, as shown in Figures 5.1c and 5.1d. The testing results validate the simulations that are presented in this work on improving the structural integrity and mechanical properties of Si anodes through GB sliding induced by Al, which further retains cycling performance.

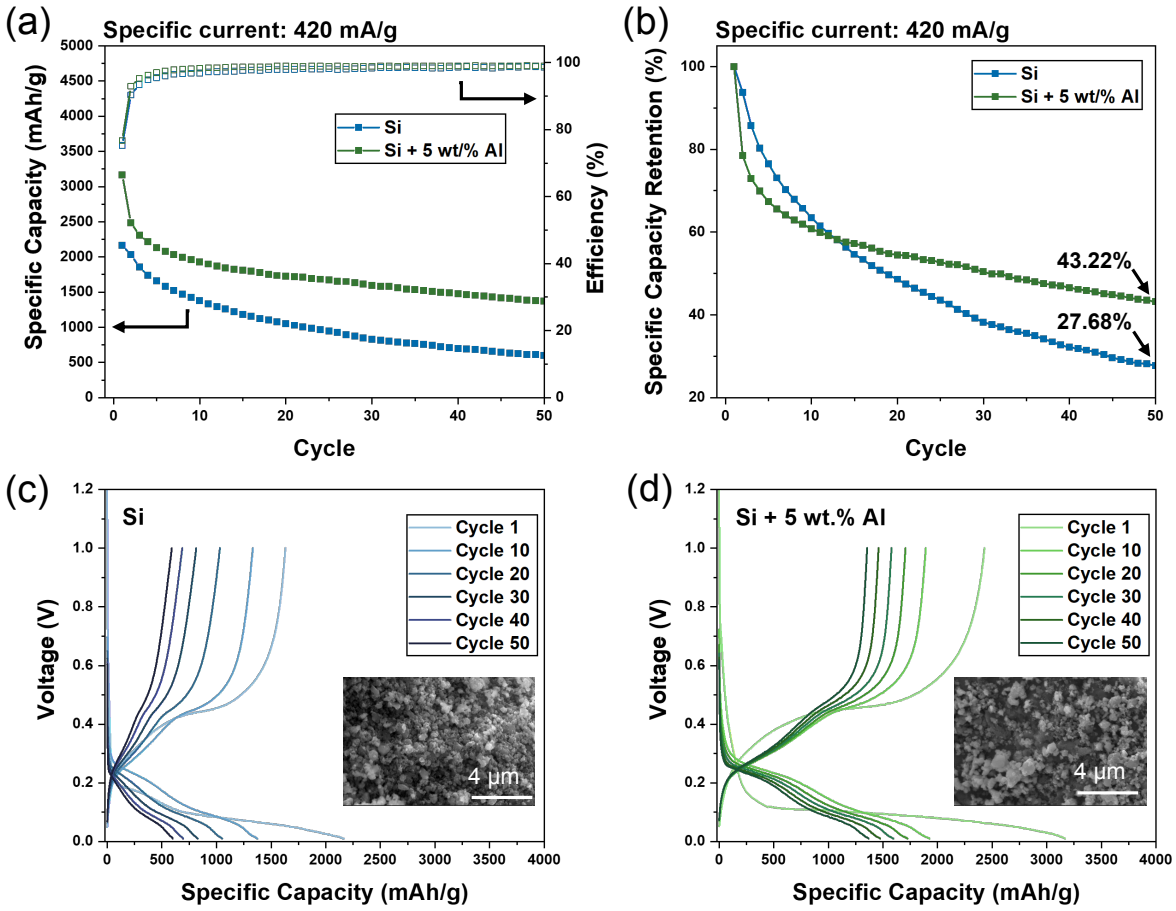

Figure 5.1: The cycling stability test of pristine high-energy-ball-milled Si and Si with 5 wt.% Al dopant. (a) Specific discharge capacity (left) with coulombic efficiency profiles (right) and (b) normalized capacity retention of pristine ball-milled Si (blue) and Si with 5 wt.% Al (green) at 0.1C. The charge/discharge voltage profiles of (c) pristine ball-milled Si and (d) Si + 5 wt.% Al with insets of secondary electron images of as-milled powders.

CHAPTER 6

Summary and Conclusion

This study presents a theoretical investigation into the impact of trace aluminum doping on grain boundary sliding, an important phenomenon dictating the mechanical stability in micro-crystalline silicon electrodes for Li-ion batteries. A grain boundary sliding model is developed and validated using density functional theory (DFT), demonstrating its consistency with previous findings. Basin hopping, a global optimization technique, is used to identify the most favorable aluminum segregation configuration. Subsequent sliding simulations revealed the facilitation of GB sliding and prevention of stress build-up in doped compared to undoped silicon. Notably, a strong dependence on aluminum concentration was observed at lower concentrations and a diminishing dependence at higher concentrations, confirming the effectiveness of trace doping. COHP analysis revealed weaker Si-Al bonds compared to Si-Si bonds as the mechanism behind improved sliding and reduced stress accumulation. Experimental capacity retention tests on a 5 wt.% Al-doped micro-crystalline silicon sample were performed by Shu-Ting Ko at the University of California San Diego in the research group of Prof. Jian Luo. These tests corroborated the theoretical predictions, showing significantly enhanced cyclic stability and material decay reduction. These findings highlight the potential of trace aluminum doping to improve Li-ion battery performance. Moving beyond aluminum, this theoretical framework opens avenues for exploring a vast variety of potential doping materials, fostering the development of next-generation Li-ion batteries with vastly improved performance and stability.

Bibliography

[1] Wu, H.; Cui, Y. Designing nanostructured Si anodes for high energy lithium ion batteries. *Nano today* **2012**, *7*, 414–429.

[2] Murray, J.; McAlister, A. The Al-Si (aluminum-silicon) system. *Bulletin of alloy phase diagrams* **1984**, *5*, 74–84.

[3] Kim, M. G.; Cho, J. Reversible and high-capacity nanostructured electrode materials for Li-ion batteries. *Advanced Functional Materials* **2009**, *19*, 1497–1514.

[4] Boukamp, B.; Lesh, G.; Huggins, R. All-solid lithium electrodes with mixed-conductor matrix. *Journal of the Electrochemical Society* **1981**, *128*, 725.

[5] Shukla, A.; Prem Kumar, T. Materials for next-generation lithium batteries. *Current science* **2008**, *94*, 314–331.

[6] Beaulieu, L.; Eberman, K.; Turner, R.; Krause, L.; Dahn, J. Colossal reversible volume changes in lithium alloys. *Electrochemical and Solid-State Letters* **2001**, *4*, A137.

[7] Kasavajjula, U.; Wang, C.; Appleby, A. J. Nano-and bulk-silicon-based insertion anodes for lithium-ion secondary cells. *Journal of power sources* **2007**, *163*, 1003–1039.

[8] Ryu, J. H.; Kim, J. W.; Sung, Y.-E.; Oh, S. M. Failure modes of silicon powder negative electrode in lithium secondary batteries. *Electrochemical and solid-state letters* **2004**, *7*, A306.

[9] Rahman, M. A.; Song, G.; Bhatt, A. I.; Wong, Y. C.; Wen, C. Nanostructured silicon anodes for high-performance lithium-ion batteries. *Advanced Functional Materials* **2016**, *26*, 647–678.

[10] Huggins, R. A. Lithium alloy negative electrodes. *Journal of Power Sources* **1999**, *81*, 13–19.

[11] McDowell, M. T.; Lee, S. W.; Wang, C.; Cui, Y. The effect of metallic coatings and crystallinity on the volume expansion of silicon during electrochemical lithiation/delithiation. *Nano Energy* **2012**, *1*, 401–410.

[12] Zuo, X.; Zhu, J.; Müller-Buschbaum, P.; Cheng, Y.-J. Silicon based lithium-ion battery anodes: A chronicle perspective review. *Nano Energy* **2017**, *31*, 113–143.

[13] Magasinski, A.; Dixon, P.; Hertzberg, B.; Kvit, A.; Ayala, J.; Yushin, G. High-performance lithium-ion anodes using a hierarchical bottom-up approach. *Nature materials* **2010**, *9*, 353–358.

[14] Kim, W.-S.; Hwa, Y.; Shin, J.-H.; Yang, M.; Sohn, H.-J.; Hong, S.-H. Scalable synthesis of silicon nanosheets from sand as an anode for Li-ion batteries. *Nanoscale* **2014**, *6*, 4297–4302.

[15] Jung, H.; Kim, Y.-U.; Sung, M.-S.; Hwa, Y.; Jeong, G.; Kim, G.-B.; Sohn, H.-J. Nanosize Si anode embedded in super-elastic nitinol (Ni–Ti) shape memory alloy matrix for Li rechargeable batteries. *Journal of Materials Chemistry* **2011**, *21*, 11213–11216.

[16] Hwang, C.-M.; Lim, C.-H.; Yang, J.-H.; Park, J.-W. Electrochemical properties of negative SiMox electrodes deposited on a roughened substrate for rechargeable lithium batteries. *Journal of Power Sources* **2009**, *194*, 1061–1067.

[17] Li, T.; Cao, Y.; Ai, X.; Yang, H. Cycleable graphite/FeSi6 alloy composite as a high

capacity anode material for Li-ion batteries. *Journal of Power Sources* **2008**, *184*, 473–476.

[18] Chen, Y.; Qian, J.; Cao, Y.; Yang, H.; Ai, X. Green synthesis and stable Li-storage performance of FeSi2/Si@ C nanocomposite for lithium-ion batteries. *ACS applied materials & interfaces* **2012**, *4*, 3753–3758.

[19] Yan, J.; Huang, H.; Zhang, J.; Yang, Y. The study of Mg2Si/carbon composites as anode materials for lithium ion batteries. *Journal of power sources* **2008**, *175*, 547–552.

[20] Zhang, R.; Du, Y.; Li, D.; Shen, D.; Yang, J.; Guo, Z.; Liu, H. K.; Elzatahry, A. A.; Zhao, D. Highly reversible and large lithium storage in mesoporous Si/C nanocomposite anodes with silicon nanoparticles embedded in a carbon framework. *Advanced Materials* **2014**, *26*, 6749–6755.

[21] Hwa, Y.; Kim, W.-S.; Hong, S.-H.; Sohn, H.-J. High capacity and rate capability of core–shell structured nano-Si/C anode for Li-ion batteries. *Electrochimica Acta* **2012**, *71*, 201–205.

[22] Liu, N.; Wu, H.; McDowell, M. T.; Yao, Y.; Wang, C.; Cui, Y. A yolk-shell design for stabilized and scalable Li-ion battery alloy anodes. *Nano letters* **2012**, *12*, 3315–3321.

[23] Liu, P.; Zheng, J.; Qiao, Y.; Li, H.; Wang, J.; Wu, M. Fabrication and characterization of porous Si-Al films anode with different macroporous substrates for lithium-ion batteries. *Journal of Solid State Electrochemistry* **2014**, *18*, 1799–1806.

[24] He, Y.; Yu, X.; Wang, Y.; Li, H.; Huang, X. Alumina-coated patterned amorphous silicon as the anode for a lithium-ion battery with high Coulombic efficiency. *Advanced materials* **2011**, *23*, 4938–4941.

[25] Tesfaye, A. T.; Gonzalez, R.; Coffer, J. L.; Djenizian, T. Porous silicon nanotube arrays as

anode material for Li-ion batteries. *ACS applied materials & interfaces* **2015**, *7*, 20495–20498.

[26] Cho, J. Porous Si anode materials for lithium rechargeable batteries. *Journal of Materials Chemistry* **2010**, *20*, 4009–4014.

[27] Kim, H.; Kweon, K. E.; Chou, C.-Y.; Ekerdt, J. G.; Hwang, G. S. On the nature and behavior of Li atoms in Si: A first principles study. *The Journal of Physical Chemistry C* **2010**, *114*, 17942–17946.

[28] Johari, P.; Qi, Y.; Shenoy, V. B. The mixing mechanism during lithiation of Si negative electrode in Li-ion batteries: an ab initio molecular dynamics study. *Nano letters* **2011**, *11*, 5494–5500.

[29] Chan, M. K.; Wolverton, C.; Greeley, J. P. First principles simulations of the electrochemical lithiation and delithiation of faceted crystalline silicon. *Journal of the American Chemical Society* **2012**, *134*, 14362–14374.

[30] Rahaman, O.; Mortazavi, B.; Rabczuk, T. A first-principles study on the effect of oxygen content on the structural and electronic properties of silicon suboxide as anode material for lithium ion batteries. *Journal of Power Sources* **2016**, *307*, 657–664.

[31] Chou, C.-Y.; Hwang, G. S. Role of interface in the lithiation of silicon-graphene composites: A first principles study. *The Journal of Physical Chemistry C* **2013**, *117*, 9598–9604.

[32] Stournara, M. E.; Qi, Y.; Shenoy, V. B. From ab initio calculations to multiscale design of Si/C core–shell particles for Li-ion anodes. *Nano letters* **2014**, *14*, 2140–2149.

[33] Kim, S.-Y.; Ostadhossein, A.; Van Duin, A. C.; Xiao, X.; Gao, H.; Qi, Y. Self-generated concentration and modulus gradient coating design to protect Si nano-wire electrodes during lithiation. *Physical Chemistry Chemical Physics* **2016**, *18*, 3706–3715.

[34] Kulish, V. V.; Malyi, O. I.; Ng, M.-F.; Wu, P.; Chen, Z. Enhanced Li adsorption and diffusion in silicon nanosheets based on first principles calculations. *Rsc Advances* **2013**, *3*, 4231–4236.

[35] Charapale, O.; Dhamija, S.; Garg, A. A theoretical study of aluminium doping in silicon anode based lithium-ion batteries using ReaxFF molecular dynamics simulation. *International Journal of Energy Research* **2022**, *46*, 3714–3724.

[36] Wang, Z.; Su, Q.; Deng, H.; Fu, Y. Composition dependence of lithium diffusion in lithium silicide: a density functional theory study. *ChemElectroChem* **2015**, *2*, 1292–1297.

[37] Soto, F.; de la Hoz, J. M.; Seminario, J.; Balbuena, P. Modeling solid-electrolyte interfacial phenomena in silicon anodes. *Current Opinion in Chemical Engineering* **2016**, *13*, 179–185.

[38] Martinez de la Hoz, J. M.; Leung, K.; Balbuena, P. B. Reduction mechanisms of ethylene carbonate on Si anodes of lithium-ion batteries: effects of degree of lithiation and nature of exposed surface. *ACS applied materials & interfaces* **2013**, *5*, 13457–13465.

[39] Ma, Y.; Balbuena, P. B. DFT study of reduction mechanisms of ethylene carbonate and fluoroethylene carbonate on Li+-adsorbed Si clusters. *Journal of the Electrochemical Society* **2014**, *161*, E3097.

[40] Wang, A.; Kadam, S.; Li, H.; Shi, S.; Qi, Y. Review on modeling of the anode solid electrolyte interphase (SEI) for lithium-ion batteries. *NPJ Computational materials* **2018**, *4*, 15.

[41] Meyers, M. A.; Mishra, A.; Benson, D. J. Mechanical properties of nanocrystalline materials. *Progress in materials science* **2006**, *51*, 427–556.

[42] Ashby, M. Boundary defects, and atomistic aspects of boundary sliding and diffusional creep. *Surface Science* **1972**, *31*, 498–542.

[43] Weinberg, F. Grain boundary shear in aluminum. *Acta Metallurgica* **1954**, *2*, 889–890.

[44] Bell, R.; Langdon, T. An investigation of grain-boundary sliding during creep. *Journal of Materials Science* **1967**, *2*, 313–323.

[45] Adsit, N.; Brittain, J. GRAIN BOUNDARY SLIDING VERSUS GRAIN BOUNDARY MIGRATION IN CREEP. 1960.

[46] Puttick, K.; King, R. Boundary Slip in Bicrystals of Tin. *Journal of the Institute of Metals* **1952**, *80*, 537.

[47] Intrater, J.; Machlin, E. A method for growing bicrystals of copper. *AIME TRANS* **1959**, *215*, 471–472.

[48] Maji, R.; Luppi, E.; Capron, N.; Degoli, E. Ab initio study of oxygen segregation in silicon grain boundaries: The role of strain and vacancies. *Acta Materialia* **2021**, *204*, 116477.

[49] Käshammer, P.; Sinno, T. Interactions of twin boundaries with intrinsic point defects and carbon in silicon. *Journal of Applied Physics* **2013**, *114*, 083505.

[50] Chen, J.; Sekiguchi, T. Carrier Recombination Activity and Structural Properties of Small-Angle Grain Boundaries in Multicrystalline Silicon. *Japanese Journal of Applied Physics* **2007**, *46*, 6489, Publisher: IOP Publishing.

[51] Bhimineni, S. H.; Ko, S.-T.; Xia, Y.; Luo, J.; Sautet, P. First Principles Study of Aluminum Doped Polycrystalline Silicon as a Potential Anode Candidate in Li-ion Batteries. *ChemRxiv* **2024**,

[52] Kresse, G.; Hafner, J. Ab initio molecular dynamics for liquid metals. *Physical review B* **1993**, *47*, 558.

[53] Larsen, A. H.; Mortensen, J. J.; Blomqvist, J.; Castelli, I. E.; Christensen, R.; Dułak, M.; Friis, J.; Groves, M. N.; Hammer, B.; Hargus, C.; others The atomic simulation environ-

ment—a Python library for working with atoms. *Journal of Physics: Condensed Matter* **2017**, *29*, 273002.

[54] Bhimineni, S. H.; Xia, Y. Scalar Codes. `https://github.com/sreeharshab/scalar_codes`.

[55] Perdew, J. P.; Burke, K.; Ernzerhof, M. Generalized gradient approximation made simple. *Physical review letters* **1996**, *77*, 3865.

[56] Monkhorst, H. J.; Pack, J. D. Special points for Brillouin-zone integrations. *Physical review B* **1976**, *13*, 5188.

[57] Zheng, H.; Li, X.-G.; Tran, R.; Chen, C.; Horton, M.; Winston, D.; Persson, K. A.; Ong, S. P. Grain Boundary Properties of Elemental Metals. 2019; `https://arxiv.org/abs/1907.08905`.

[58] Tschopp, M. A.; Coleman, S. P.; McDowell, D. L. Symmetric and asymmetric tilt grain boundary structure and energy in Cu and Al (and transferability to other fcc metals). *Integrating Materials and Manufacturing Innovation* **2015**, *4*, 176–189.

[59] Wales, D. J.; Doye, J. P. Global optimization by basin-hopping and the lowest energy structures of Lennard-Jones clusters containing up to 110 atoms. *The Journal of Physical Chemistry A* **1997**, *101*, 5111–5116.

[60] Metropolis, N.; Ulam, S. The monte carlo method. *Journal of the American statistical association* **1949**, *44*, 335–341.

[61] Sun, G.; Alexandrova, A. N.; Sautet, P. Pt8 cluster on alumina under a pressure of hydrogen: Support-dependent reconstruction from first-principles global optimization. *The Journal of chemical physics* **2019**, *151*.

[62] Okada, Y.; Tokumaru, Y. Precise determination of lattice parameter and thermal expansion coefficient of silicon between 300 and 1500 K. *Journal of applied physics* **1984**, *56*, 314–320.

[63] Ratanaphan, S.; Yoon, Y.; Rohrer, G. S. The five parameter grain boundary character distribution of polycrystalline silicon. *Journal of materials science* **2014**, *49*, 4938–4945.

[64] Ivanov, V.; Mishin, Y. Dynamics of grain boundary motion coupled to shear deformation: An analytical model and its verification by molecular dynamics. *Physical Review B* **2008**, *78*, 064106.

[65] Wan, L.; Wang, S. Shear response of the Σ 9 $\langle 110 \rangle \{221\}$ symmetric tilt grain boundary in fcc metals studied by atomistic simulation methods. *Physical Review B* **2010**, *82*, 214112.

[66] Maintz, S.; Deringer, V. L.; Tchougréeff, A. L.; Dronskowski, R. LOBSTER: A tool to extract chemical bonding from plane-wave based DFT. 2016.